RSC Advances

ROYAL SOCIETY OF CHEMISTRY

PAPER

View Article Online
View Journal | View Issue

Check for updates

Cite this: *RSC Adv.*, 2021, **11**, 28042

Exploring the electrochemical performance of copper-doped cobalt–manganese phosphates for potential supercapattery applications†

Meshal Alzaid,*[a] Muhammad Zahir Iqbal, *[b] Saman Siddique[b] and N. M. A. Hadia[a]

The significant electrochemical performance in terms of both specific energy and power delivered *via* hybrid energy storage devices (supercapattery) has raised their versatile worth but electrodes with flashing electrochemical conduct are still craved for better performance. In this work, binary and ternary metal phosphates based on copper, cobalt, and manganese were synthesized by a sonochemical method. Then, the compositions of copper and cobalt were optimized in ternary metal phosphates. The structural studies and morphological aspects of synthesized materials were scrutinized by X-ray diffraction and scanning electron microscopy. Furthermore, the electrochemical characterizations were performed in three- and two-cell configurations. The sample with equal compositions of copper and cobalt (50/50) demonstrates the highest specific capacity of 340 C g^{-1} at a current density of 0.5 A g^{-1} among all. This optimized composition was utilized as a positive electrode material in a supercapattery device that reveals a high specific capacity of 247 C g^{-1}. The real device exhibits an excellent energy density of 55 W h kg^{-1} while delivering a power density of 800 W kg^{-1}. Furthermore, the device was able to provide an outstanding specific power of 6400 W kg^{-1} while still exhibiting a specific energy of 19 W h kg^{-1}. The stability potential of the device was tested for 2500 continuous charge and discharge cycles at 8 A g^{-1}. Excellent capacitive retention of 90% was obtained, which expresses outstanding cyclic stability of the real device. A theoretical study was performed to investigate the capacitance and diffusion-controlled contribution in the device performance using Dunn's model. The maximum diffusion-controlled contribution of 85% was found at 3 mV s^{-1} scan rate. The study demonstrates the utilization of ternary metal phosphates as self-supported electrode materials for potential energy storage applications.

Received 24th November 2020
Accepted 8th May 2021

DOI: 10.1039/d0ra09952j

rsc.li/rsc-advances

1. Introduction

The high rate exhaustion of fossil fuels and increasing energy consumption necessitate the search for renewable energy resources. To maintain a balance between energy demand and supply, progression toward advanced energy storage systems is equally required.[1,2] Presently, electrochemical supercapacitors (SCs) are the emerging energy devices because of their properties such as rapid charge–discharge and enhanced power density with a long lifespan. The charge storage mechanism categorized them into two types, *i.e.* EDLCs in which charge stores due to physical adsorption and pseudocapacitors in which surface redox reactions within a finite potential range are involved. The low energy density of SCs as compared to other energy storage devices such as batteries limits their broader commercial applications. To address the mentioned limitation, it is necessary to design an efficient and high-performance energy storage device with increased energy density (to compete with the requirement) while retaining the high power density.[3,4] This was accomplished *via* another class of SCs that are called hybrid supercapacitors, also termed supercapattery. In these devices, battery as well as capacitive grade electrode materials are constraints in a single device.[5] This results in enhanced energy density due to the faradaic reaction (due to battery-grade material) and outstanding power density due to the non-faradaic charge storage phenomena (*via* insertion of capacitive material).[6,7] For these superstitious merits, charge storage has gained vital interest of researchers at present.

Different types of capacitive (negative electrode) and battery-grade (positive electrode) materials have been extensively utilized for hybrid SCs. Among EDLCs, carbon-enriched materials such as activated carbon,[8,9] graphene,[10,11] and its composites[12] have been mostly utilized as active materials in the negative electrode. The most commonly used positive electrode materials are transition metal oxides,[13–16] metal hydroxides,[17,18]

---

[a] *Physics Department College of Science, Jouf University, P. O. Box 2014, Sakaka, Al Jouf, Saudi Arabia*

[b] *Nanotechnology Research Laboratory, Faculty of Engineering Sciences, GIK Institute of Engineering Sciences and Technology, Topi 23640, Khyber Pakhtunkhwa, Pakistan. E-mail: zahir.upc@gmail.com; mmalzaid@ju.edu.sa*

† Electronic supplementary information (ESI) available. See DOI: 10.1039/d0ra09952j

mixed metal sulfides,[19–22] and phosphates.[23–28] Among these materials, metal phosphates and phosphides have been explored as suitable candidates.[29] Their low cost, chemical stability, redox-active nature, and excellent electrochemical properties make them more feasible for efficient SC devices.[30] Among various phosphates and phosphides, manganese and cobalt phosphates are intensively studied for SC applications due to high capacitance, thermal and electrochemical stability, and excellent electrochemical activities.[28,31–34] For example, Mirghni *et al.* synthesized $MnPO_4$ nanorods *via* utilizing the hydrothermal process and investigated the behavior of $MnPO_4$ by different mass loadings on graphene foam.[31] The highest capacitance was found to be 270 F g^{-1} at 0.5 A g^{-1} using an operating voltage window of 1.4 V in 6 M KOH electrolyte. The material also demonstrates maximum capacity preservation of 96% after 10 000 continuous cycles at 2 A g^{-1}. Similarly, cobalt phosphates and phosphides were analyzed due to high electronic, magnetic and catalytic properties. Cobalt phosphates are excessively used for electrode materials in high-performance SC devices. Chen *et al.* reported the nano-flower-shaped CoP exhibiting a capacitance of 418 F g^{-1} at 1 A g^{-1}.[35] The energy and power densities were observed to be 8.8 W h kg^{-1} and 6 W kg^{-1}, respectively, with good cyclic durability of 97% for 6000 cycles. Furthermore, along with other transition metals, copper phosphide also holds sound electrocatalytic properties. Chen *et al.* have synthesized copper phosphide nanotubes *via* an electro-oxidation route and investigated the electrochemical characteristics.[36] The asymmetric device was designed by using the copper phosphide electrode as the anode, which delivers a significant specific energy of 44.6 W h kg^{-1} and a specific power of 17 kW kg^{-1} with cyclic stability of 81.9% after 5000 charge/discharge cycles. Inspired by the attractive properties of these metal phosphates, a drive toward mixed metal phosphate composite could result in an electrode material with flashing electrochemical performance and durability.

Herein, we present the synthesis of binary and ternary metal phosphates at different aspects ratios by the sonochemical technique. The structural and morphological studies were investigated by X-ray diffraction and scanning electron microscopy (SEM). Electrochemical characterizations were performed in a three-cell configuration to scrutinize the performance optimization of the synthesized materials. The electrode material with the finest electrochemical conduct was further utilized for supercapattery applications along with activated carbon. The fabricated device was electrochemically tested in a two-electrode assembly by different characterizations. The stability and durability of the device were also analyzed. Furthermore, theoretical studies based on Dunn's model were also performed to investigate the capacitance-controlled contribution. The study paves a new way to explore ternary metal phosphates for high-performance supercapattery applications.

2. Experimental methods

2.1. Materials

Copper(II) chloride ($CuCl_2$), cobalt chloride ($CoCl_2$. $6H_2O$), and manganese(II) chloride ($MnCl_2$) were bought from MERCK. Potassium hydroxide (KOH), disodium hydrogen phosphate (Na_2HPO_4), hydrochloric acid (HCl), ethanol, *N*-methyl-2-pyrrolidone (NMP), *N*-poly-vinylidene fluoride (PVDF), acetone, activated carbon (AC), and carbon black were purchased from Sigma Aldrich. Nickel foam was procured from Urich Technology, Malaysia. Deionized (DI) water was purchased from a scientific store for the preparation of precursor solutions and electrolytes.

The electrochemical performance of the as-prepared samples was evaluated in a three-electrode configuration, where a Pt wire and a Hg/HgO electrode purchased from ALS Co., Ltd, Japan were utilized as the counter and reference electrodes respectively.

2.2. Synthesis of binary metal phosphates

Initially, binary metal phosphates ($CuMnPO_4$) and ($CoMnPO_4$) were synthesized by adopting the sonochemical technique. To synthesize $CuMnPO_4$, a 0.3 M solution of Na_2HPO_4 was made in 50 ml DI water. Two separate precursor solutions of 0.5 M $CuCl_2$ and 0.5 M $MnCl_2$ were prepared and mixed in an ultrasonic bath. The precursor solution was then placed in a probe sonicator and a Na_2HPO_4 solution was added dropwise. The process goes on for 45 minutes with an ultrasonic wave amplitude of 30%. A colloidal solution was obtained, which was centrifuged to collect the synthesized material. After washing several times with DI water and acetone to remove residue, the material was obtained and dried in a muffle furnace at 60 °C.[37] The dried material was calcined at 400 °C for 3 hours and named S1. Similarly, $CoMnPO_4$ was also prepared using 0.5 M $CoCl_2$ instead of $CuCl_2$, and the sample was named S5.

2.3. Synthesis of ternary metal phosphates

To accomplish the synthesis of copper-doped cobalt–manganese phosphates (ternary phosphate), a solution of $MnCl_2$, $CoCl_2$, and $CuCl_2$ was prepared with a molar ratio of 1 : 0.75 : 0.25 and mixed to make a 50 ml solution. This precursor solution was subjected to probe sonication and the Na_2HPO_4 solution was added drop by drop into it. The process was prolonged for 45 minutes. Later on, the material was collected, washed and then dried overnight at 60 °C. The obtained material was further calcined at 400 °C for 3 hours. The synthesized $Cu_{0.50}Mn_{0.50}PO_4$ was named S2. The molar concentration of $MnCl_2$ was kept fixed and the amount of $CoCl_2$ and $CuCl_2$ was varied in the precursor solution. The same strategy was followed for the preparation of S3 and S4 with different compositions of cobalt and copper ($Co_{0.50}Cu_{0.50}MnPO_4$ and $Co_{0.25}Cu_{0.75}MnPO_4$). Table S1† represents the names of different samples along with their concentrations. The synthesis route is schematically illustrated in Fig. 1.

2.4. Electrode preparation

The working electrode was prepared by making a slurry containing 75 wt% as-synthesized material, 15 wt% acetylene black (carbon black), and 10 wt% PVDF as a binder. The homogeneous slurry after continuous stirring for 9 hours was deposited on 1×1 cm^2 of Ni foam and placed in a muffle furnace at 90 °C for 8 hours. All electrochemical measurements were conducted in 1 M KOH electrolyte.

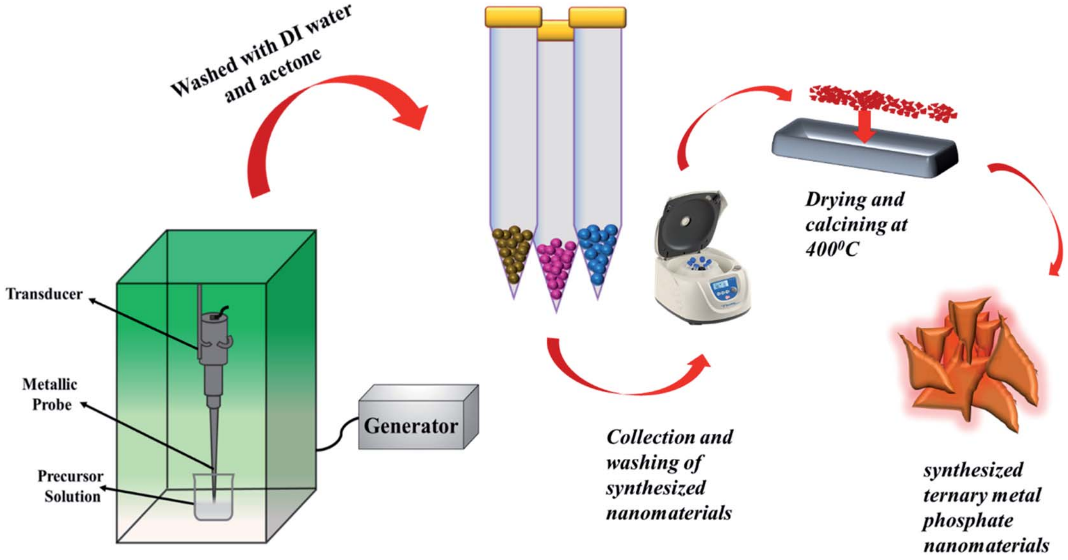

Fig. 1 Schematic of the preparation of mixed metal phosphates.

3. Results and discussion

The characterization techniques were conducted to investigate the surface morphology, structure, and electrochemical behavior of the synthesized material which are as follows:

3.1. Structural characterization

Morphological and structural characterizations were performed to investigate the phase and crystallinity of the synthesized material by scanning electron microscopy (FESEM) (JEOL JSM-7600F) and X-ray diffraction (XRD) (Bruker axis D8 Advance diffractometer, Germany) with a wavelength of 1.5406 Å at 40 kV.

3.1.1. X-ray diffraction (XRD). The structural morphology of the as-synthesized materials was identified by XRD analysis. Fig. 2(a) represents the XRD pattern of all samples. Three prominent peaks occurred at 20°, 26.5°, and 67.8° represents the formation of cobalt, copper, and manganese phosphate. Moreover, the peak positions match well with the previous reported literature.[31,38] A minor leftward shift in the XRD peak

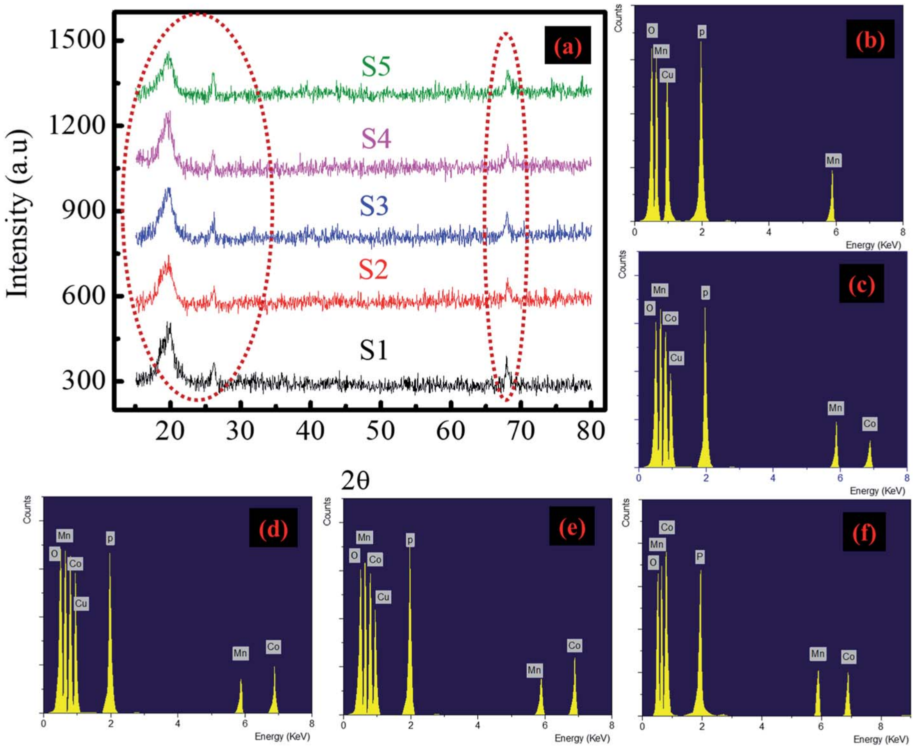

Fig. 2 (a) XRD pattern of the as-synthesized samples and (b–f) EDX spectrum of all the samples.

positions from S1 to S5 depicts the change in the crystal plane spacing, which may be due to the varying concentration of copper and cobalt in mixed metal phosphates. Moreover, the less intensity of diffraction peaks is due to the amorphous nature of the material that may facilitate electrochemical activities.[39–41]

3.1.2. Energy-dispersive X-ray spectroscopy (EDX). The EDX analysis was performed to depict the elemental analysis of all the synthesized materials. The obtained spectrum from materials S1, S2, S3, S4, and S5 was demonstrated in Fig. 2 (b–f) respectively. The EDX spectrum of S1 shows peaks at (kα) 0.53 keV, (Lα) 0.930 keV, (kα) 5.89 keV and (kα) 2.01 keV, which correspond to O, Mn, Cu and P elements correspondingly. Fig. 2(f) shows the EDX outcomes of S5, which encompasses peaks that define O (kα 0.53 keV), Mn (Lα 0.930 keV), Co (Lα 0.77 and kα 6.92 keV), and P (kα 2.01 keV) elements affirm the synthesis of cobalt–manganese phosphate. The EDX spectra of S2, S3, and S4 show the peaks that affirm the presence of O, Mn, Cu, Co, and P elements, which portray the copper-doped cobalt–manganese phosphates.

3.1.3. Scanning electron microscopy (SEM). To elucidate the surface and structural morphology of all samples, SEM measurements were performed. The results of all synthesized materials are presented in Fig. 3. The SEM images reveal the formation of nanoflakes except for S5. This flaky morphology supports the diffusion of electrolytic ions and improves charge transportation, yielding a high rate capability.[42] S5 shows a nanograin-like morphology. In mixed metal phosphates, the as-synthesized material exhibits a mixed surface morphology. For S1, S2, and S3, there was a nanoflower-like morphology due to the high concentration of copper, which facilitates the high ionic conduction,[38] whereas for S5, the particles are agglomerated, which reveals low conductivity.[43]

3.2. Electrochemical characterization

To evaluate the electrochemical behavior of the synthesized material for practical applications of SCs, electrochemical measurements were conducted using a potentiostat/galvanostat (Gamry Reference 3000). For the evaluation of electrochemical measurements, two types of electrode configurations were used: two-electrode assembly and three-electrode assembly.

3.2.1. Cyclic voltammetry. The electrochemical performance of mixed metal phosphates was evaluated by CV using a three-electrode assembly. CV measurements were conducted at various sweep rates from 3 to 50 mV s^{-1} in a potential window of 0 to 0.6 V. Fig. 4(a–e) represents the CV plots of S1, S2, S3, S4, and S5 respectively. The graphs evince the presence of coupled redox peaks, which state the occurrence of faradaic reactions

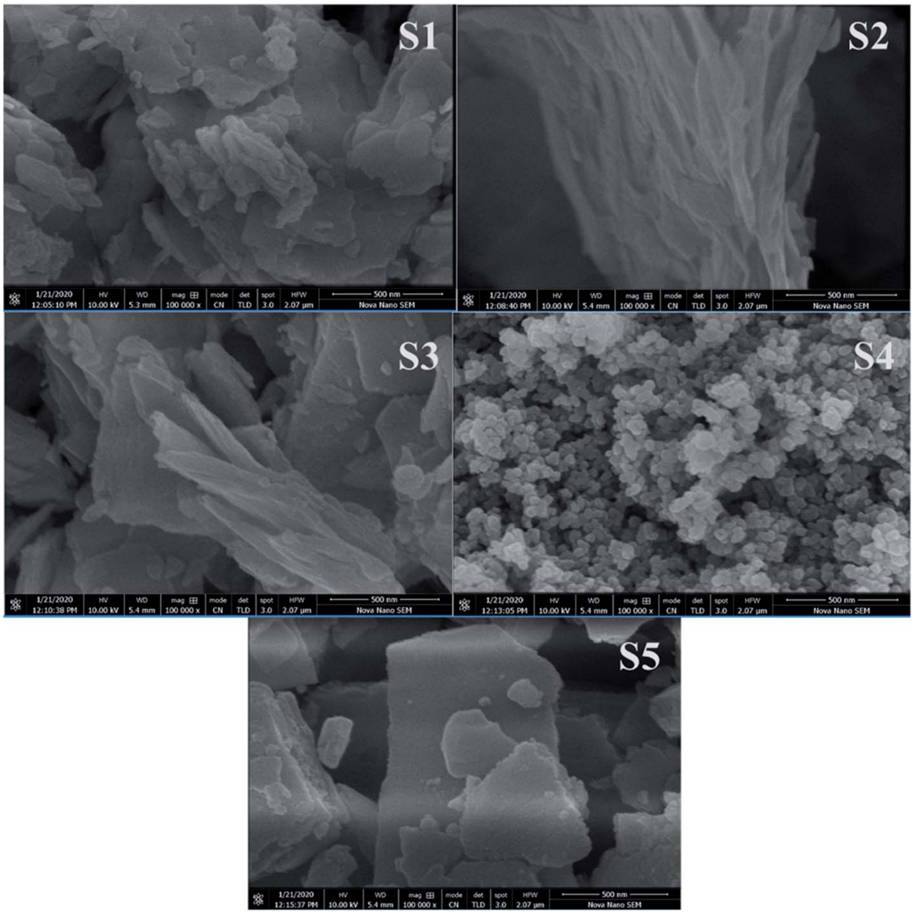

Fig. 3 SEM images of S1, S2, S3, S4 and S5.

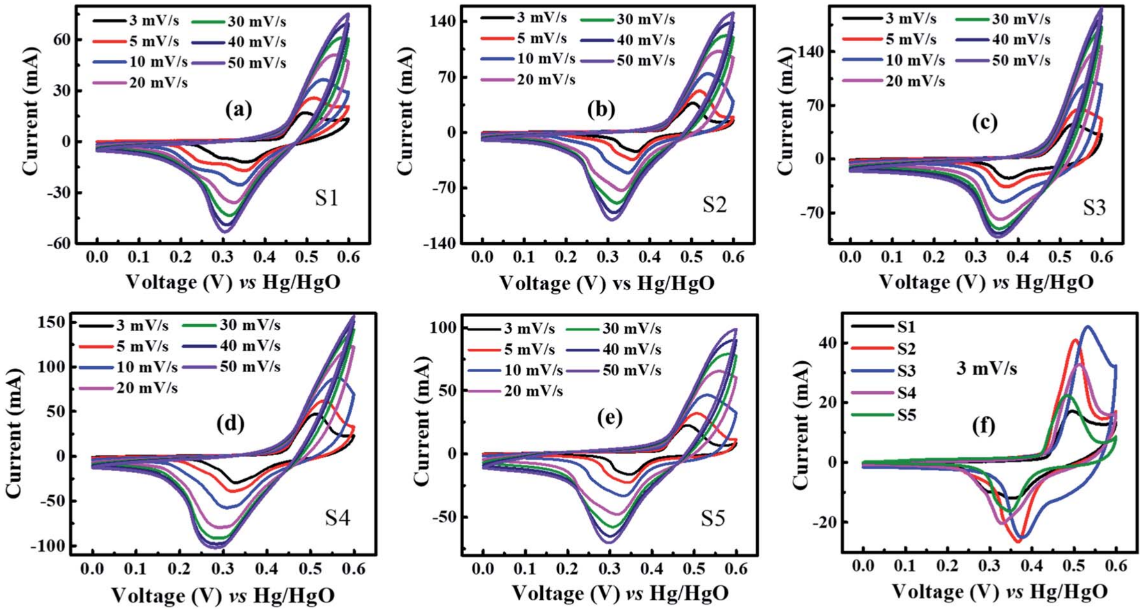

Fig. 4 CV plots of (a) S1, (b) S2, (c) S3, (d) S4, (e) S5, and (f) comparison cyclic voltammogram of all samples at 3 mV s^{-1}.

likely to battery-grade materials. The CV graphs also reveal the enhancement gradual shift of redox peak current. This is because the high values of the potential sweep rate enhance the kinetics of electrolyte ion that results in fast reactions at the electrode–electrolyte interface. Besides, the CV spectrum of each sample elucidates the redox nature and maintains high scan rates, which elaborate their outstanding rate capability. This explains the high diffusion of electrolyte ions into the electrode material, charge adsorption at the surface of the electrodes, and the charge transfer capability of the electrode material.

The specific capacity is extracted from CV curves using the following formula:

$$Q_s = \frac{1}{2mv}\int_{Vf}^{Vi} I \times V\mathrm{d}V \tag{1}$$

here, Q_s represents the specific capacity (C g^{-1}), m signifies the active material's mass (g), v is the scan rate (mV s^{-1}), and V is relates to the potential range utilized. The integral part shows the area under voltammogram. A comparison in the performance of S1, S2, S3, S4, and S5 at a fixed scan rate (3 mV s^{-1}) is plotted in Fig. 4(f), which indicates that maximum current is achieved by sample S3 having a large area under the curve. The specific capacity of all the samples calculated at different sweep rates is elaborated in Fig. 5. S1, S2, S3, S4, and S5 exhibit a maximum capacity of 206.4, 404.8, 416.2, 290.8, and 178.01 C g^{-1} at 3 mV s^{-1}. The specific capacity of the electrode gradually decreases at high sweep rates. This is because the ionic diffusion at the electrode/electrolyte interface and the charge transportation of ions through the electrolyte is limited at high scan rates, which results in decreased specific capacity.[27] In the light of above-mentioned discussion, sample S3 (having an equal concentration of copper and cobalt) demonstrates better stability and high specific capacity as compared to all other samples.

3.2.2. Galvanostatic charge/discharge. The electrochemical behavior of mixed metal phosphates was investigated by performing GCD within a voltage range of 0 to 0.5 V at different current densities from 0.5 to 4 A g^{-1} in KOH electrolyte. Fig. 6(a–e) illustrates the GCD curves of all samples *i.e.* S1, S2, S3, S4, and S5 at different current densities. Nonlinear behavior is observed in the charge/discharge curves, which indicate the battery-grade nature of the electrode material. The starting and end positions of the curves display a linear line, confirming the capacitive storage at the electrode/electrolyte interface. In contrast, the non-linear part shows the redox reactions within the electrolyte.

The specific capacity was calculated from GCD plots using the following equation:[27]

$$Q_s = \frac{I \times \Delta t}{m} \tag{2}$$

here, Δt (discharging time) is expressed in seconds. Fig. 6(e) represents the comparison of GCD curves of all the samples at 5 A g^{-1}, which elucidates the dominant behavior of S3 with

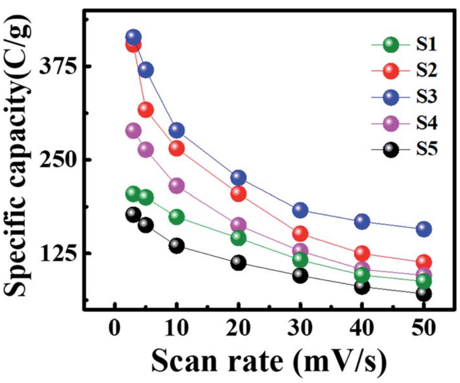

Fig. 5 Specific capacity of all the samples at multiple scan rates.

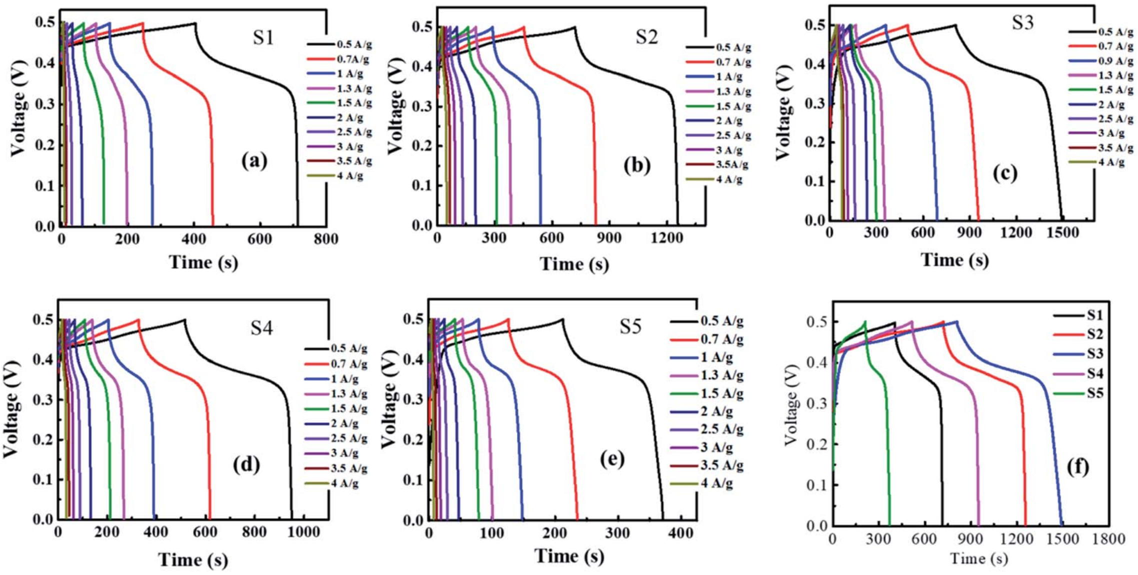

Fig. 6 GCD graphs of (a) S1, (b) S2, (c) S3, (d) S4, (e) S5, and (f) comparison of GCD curves of all samples.

more discharge time. Fig. 7 shows the specific capacity extracted from the discharging curves of all samples as a function of current densities varying from 0.5 A g^{-1} to 4 A g^{-1}. Fig. S1† illustrates the comparative analysis of maximum specific capacity provided by all the samples, which reveal that S3 exhibits the highest specific capacity value of 341 C g^{-1} at 0.5 A g^{-1}. The GCD discussion evinces the prime electrochemical performance of S3.

3.2.3. Electrochemical impedance spectroscopy. To calculate the equivalent series resistance (ESR) and investigate the conductive properties of electrode materials, EIS measurements were conducted employing a frequency range of 0.1 Hz to 10^5 Hz. Fig. 8 demonstrates the Nyquist plot of the EIS results for all the samples. The inset represents the sharp frequency region to observe the real axis intercept (ESR). It can be observed from the Nyquist plot that the minimum resistance is offered by the sample S3 which confirms its highest conductivity as compared to all other samples. Moreover, the diameter of the EIS curve in sharp frequency range depicts the charge transfer resistance (R_{ct}), which occurs due to the transfer of ions in the electrolyte. The spectrum of all the samples exhibits a very small semicircular nature in the high-frequency region and, thus, has a low value of R_{ct}. At low-frequency regime, the straight line indicates the Warburg impedance (W_d) that originated from the diffusion of electrolytic ions into the electrode material.[43] The line for S3 shows less deviation and represents low Warburg impedance as compared to S2 and S4. Moreover, the ESR value of S1, S2, S3, S4 and S5 is presented in Fig. S2.† The above-mentioned results agree well with the experimental results of CV and GCD, which confirms better electrochemical performance of S3 than that of the other four samples.

3.2.4. Evaluation of supercapattery device. The real device performance of the optimized electrode material (S3) was evaluated. In this regard, an asymmetric (supercapattery) device was fabricated utilizing active material S3 as the anodic material (positive electrode) and activated carbon (AC) as the cathodic material (negative electrode). A porous membrane was used to provide separation. The supercapattery device is schematically represented in Fig. 9(a). The individual CV of AC and S3 performed in a three-electrode assembly is demonstrated in Fig. 9(b). The working potential range for AC is from −1 to 0 and

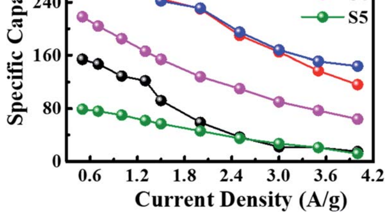

Fig. 7 Specific capacity of all samples *versus* current density.

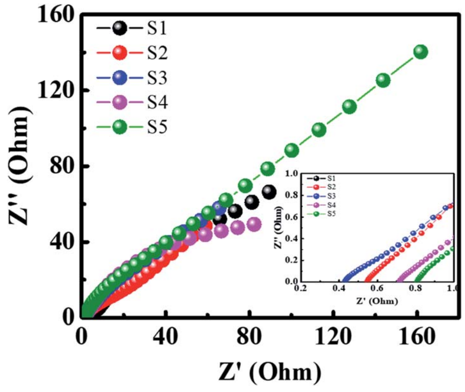

Fig. 8 Nyquist plot of EIS for all samples.

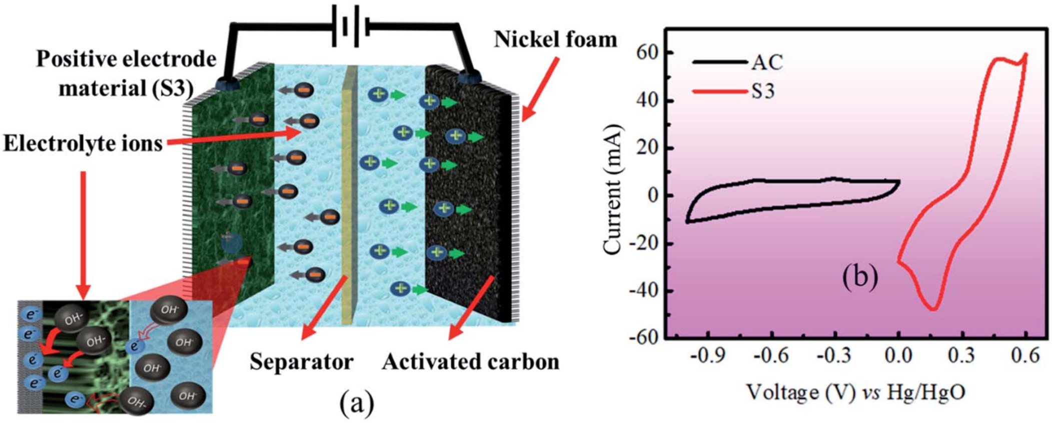

Fig. 9 (a) Schematic of asymmetric supercapattery device and (b) CV plots of activated carbon and mixed metal phosphates.

for active material S3, the potential range is from 0 to 0.6. This depicts that the reliable orating voltage range for supercapattery device is 0 to 1.6 V. Furthermore, the CV curve of AC shows a quasi-rectangular behavior, which depicts the EDLC charge storage mechanism, whereas S3 shows the corresponding redox peaks, which affirm the battery-grade behavior.

Fig. 10(a) shows the cyclic voltammogram of supercapattery device at different voltage windows to optimize the maximum operating voltage range. The CV graphs of supercapattery devices using different operating voltages range up to 0–1.6 V. The CV spectrum contains both EDLC and battery grade behavior due to asymmetric device architecture. Moreover, no distortion in CV shape evinces the reliability of this broad potential window of 0–1.6 V. The CV measurements of the real device are performed at different sweep rates from 3 to 100 mV s^{-1}, and cyclic voltammogram is presented in Fig. 10(b). It can be seen that the real device maintains its CV shape even up to higher sweep rates. This suggests good rate capability and electrochemical stability of the supercapattery device.

Similarly, GCD measurements for the supercapattery device, performed at different potential windows, are represented in Fig. 10(c). This again affirms that the reliable voltage range for

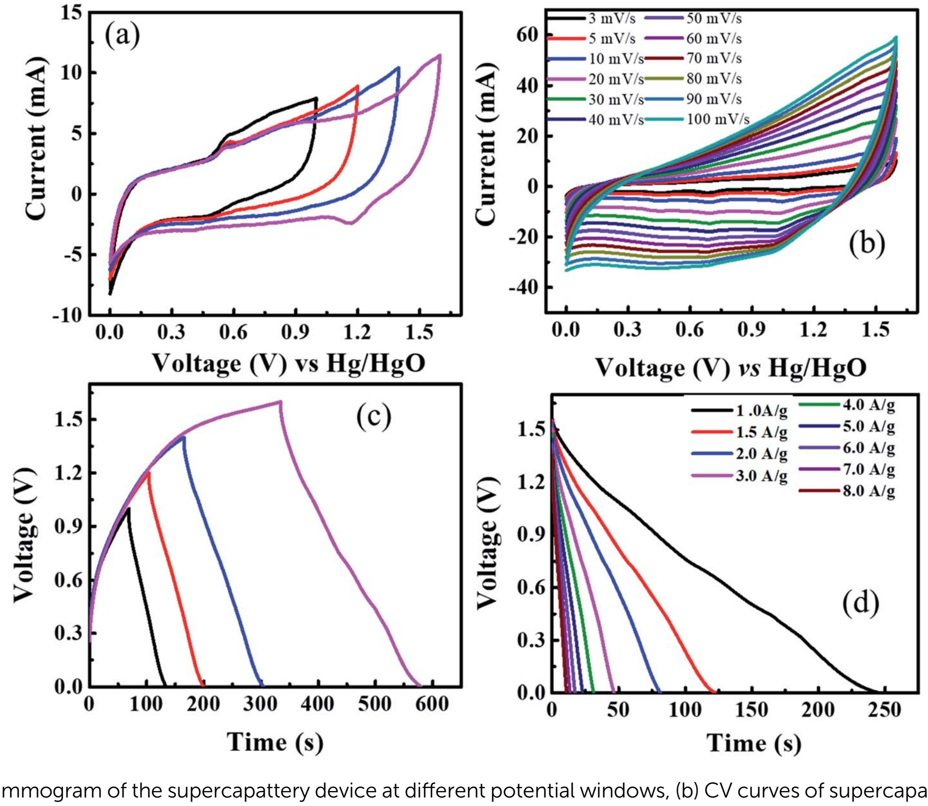

Fig. 10 (a) Cyclic voltammogram of the supercapattery device at different potential windows, (b) CV curves of supercapattery device at different scan rates within a potential window of 1.6 V, (c) GCD plots of supercapattery device at different potential windows, and (d) discharging curves of the device at different current densities within a potential window of 1.5 V.

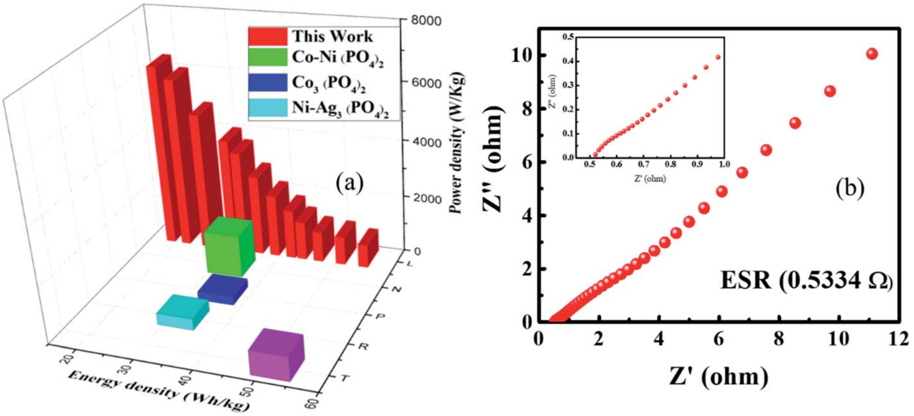

Fig. 11 (a) Specific energy and specific power of real device. (b) Nyquist plot of supercapattery device.

GCD measurements is 0–1.6 V. The GCD measurements within a voltage window of 0–1.6 V are performed at multiple values of current densities from 1 to 8 A g^{-1}. The discharge curves are shown in Fig. 10(d). The nonlinear nature of discharge curves due to the presence of little humps in the curve confirms the incorporation of both faradaic and non-faradaic reactions due to asymmetric device architecture. The specific capacity of the device was evaluated using the GCD outcomes at different. The specific capacity of the supercapattery device was found to be 247 C g^{-1} at 1 A g^{-1} current density.

Specific energy and power of the device were calculated using the following equations:[26]

$$E\left(\mathrm{W\ h\ kg^{-1}}\right) = \frac{Q_\mathrm{s} \times \Delta V}{2 \times 3.6} \tag{3}$$

$$P\left(\mathrm{W\ kg^{-1}}\right) = \frac{E \times 3600}{\Delta t} \tag{4}$$

here E and P represent the specific energy and specific power respectively. Q_s signifies the specific capacity calculated from GCD, ΔV is the potential window utilized and Δt is the time taken by the device to discharge completely. The supercapattery device delivers an excellent specific energy of 55 W h kg^{-1}, while retaining a power density of 800 W kg^{-1}. The device provides a marvelous specific power of 6400 W kg^{-1} while still exhibiting a specific energy of 19 W h kg^{-1}. The obtained results are much superior to the previously published literature for binary and tertiary metal phosphates, which indicates the worth of our work for energy storage applications. The specific energy and specific power as compared to previously reported work are illustrated in Fig. 11(a).

Furthermore, the ESR and conductivity of the supercapattery device were evaluated by EIS measurements in the frequency range of 0.1 Hz to 10^5 Hz, as illustrated in Fig. 11(b). A low ESR value of 0.533 ohms (shown in inset) was observed, which reveals that the device exhibits excellent conductance properties. Besides, a small semicircle depicts the low R_ct value of the device.

Moreover, the electrochemical stability of the device is tested for continuous cyclic charge and discharge for 2500 cycles at 8 A g^{-1} (ref. 44) demonstrated in Fig. 12. It is evident that for the first 100 cycles, the device gets fully activated giving total capacitive retention of 106% and after 100 cycles, the device shows a gradual decline giving capacitive retention of 90% after 2500 cycles. Moreover, the b-value fitting of the device is also performed and illustrated in Fig. S3.† The device expresses the b value ranging from 0.59 to 0.64, which braces the supercapattery nature.

Furthermore, charge kinetics in the supercapattery device was explored *via* a theoretical approach[16] using the following equation:

$$i(\nu) = k_1\nu + k_2\nu^{1/2} \tag{5}$$

The equation indicates the total charge storage capacity of the supercapattery device as the sum of capacitive $k_1\nu$ and diffusion-controlled $k_2\nu^{1/2}$ contributions.

The bar chart in Fig. 13 represents the percentage contribution of capacitance and diffusion-controlled processes at different scan rates. It can be seen that at low scan rates, the diffusion-controlled contribution is dominant because of the excessive redox reaction, whereas, at a higher scan rate, ion could not get enough time to complete the reaction, and hence, the capacitive contribution dominates. The maximum diffusion-controlled contribution is 85% at the lowest scan rate and the overall diffusion-controlled contribution is dominant in the total device capacity, which confirms the major contribution

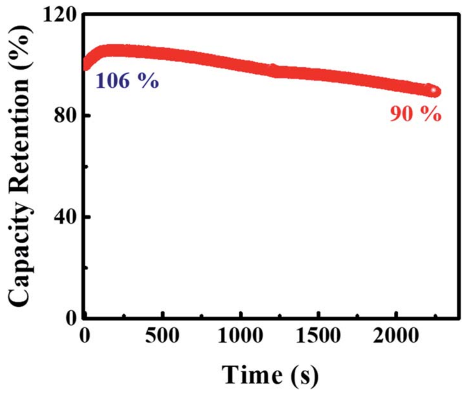

Fig. 12 Electrochemical stability of the device at 8 A g^{-1} for 1500 cycles.

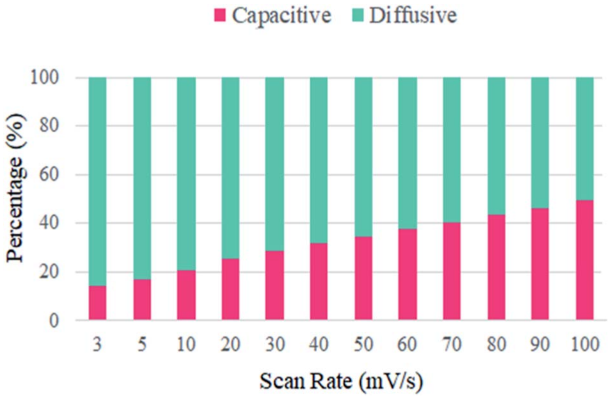

Fig. 13 Bar chart at different scan rates *versus* capacitive and diffusion-controlled contribution percentage.

of the synthesized battery-grade material in the fabricated supercapattery device.

4. Conclusion

In summary, Cu–Co–Mn-based binary and ternary phosphates with different concentrations were synthesized *via* a sonochemical route. Initially, binary metal phosphates were synthesized and then the compositions of copper and cobalt were optimized in ternary metal phosphates. The composition $Co_{0.5}Cu_{0.5}Mn(PO_4)_2$ exhibits the significant electrochemical performance in a three-electrode assembly *via* providing a specific capacity of 340 C g^{-1} at 0.5 A g^{-1}. The optimized electrode material was then utilized to fabricate a supercapattery device, which illustrates the maximum capacity of 247 C g^{-1} at 1 A g^{-1} in a two-electrode assembly. The device also provides a remarkable specific energy and power of 55 W h kg^{-1} and 800 W kg^{-1} respectively at 1 A g^{-1}. Furthermore, the device was able to provide an outstanding specific power of 6400 W kg^{-1} while still exhibiting a specific energy of 19 W h kg^{-1}. This real device also expresses capacity preservation of 90% after 2500 consecutive GCD cycles. Furthermore, the capacitance-controlled study of the supercapattery device was performed theoretically using Dunn's model, which deduced that the device exhibits an 85% diffusion-controlled contribution at 3 mV s^{-1}. Our study provides an effective progression toward the study of mixed metal phosphate-based electrode materials for high-performance supercapattery devices.

Author contributions

M. A. and M. Z. I. designed the study. S. S. and M. Z. I. performed the experiment. M. Z. I. and M. A. analyzed the data, wrote the manuscript and critically reviewed the manuscript. N. M. A. H. helped in analysis of data.

Conflicts of interest

The authors declare no financial conflict of interest.

Acknowledgements

The authors extend their appreciation to the Deanship of Scientific Research at Jouf University for funding this work through research grant no. (DSR-2021-03-0238).

References

1 A. Noori, M. F. El-Kady, M. S. Rahmanifar, R. B. Kaner and M. F. Mousavi, *Chem. Soc. Rev.*, 2019, **48**, 1272–1341.
2 M. Z. Iqbal and S. Siddique, *Int. J. Hydrogen Energy*, 2018, **43**, 21502–21523.
3 P. Simon, Y. Gogotsi and B. Dunn, *Science*, 2014, **343**, 1210–1211.
4 D. P. Dubal, O. Ayyad, V. Ruiz and P. Gomez-Romero, *Chem. Soc. Rev.*, 2015, **44**, 1777–1790.
5 M. Z. Iqbal, J. Khan, H. T. A. Awan, M. Alzaid, A. M. Afzal and S. Aftab, *Dalton Trans.*, 2020, **49**, 16715–16727.
6 B. Akinwolemiwa, C. Peng and G. Z. Chen, *J. Electrochem. Soc.*, 2015, **162**, A5054–A5059.
7 G. Z. Chen, *Prog. Nat. Sci.: Mater. Int.*, 2013, **23**, 245–255.
8 S. Yaglikci, Y. Gokce, E. Yagmur and Z. Aktas, *Environ. Technol.*, 2020, **41**, 36–48.
9 S.-K. Chang and Z. Zainal, in *Synthesis, Technology and Applications of Carbon Nanomaterials*, Elsevier, 2019, pp. 309–334.
10 W. K. Chee, H. N. Lim, Z. Zainal, N. M. Huang, I. Harrison and Y. Andou, *J. Phys. Chem. C*, 2016, **120**, 4153–4172.
11 P. Luo, X. Guan, Y. Yu, X. Li and F. Yan, *Nanomaterials*, 2019, **9**, 201.
12 Z. Yang, J. Tian, Z. Yin, C. Cui, W. Qian and F. Wei, *Carbon*, 2019, **141**, 467–480.
13 L. Wang, X. Xie, K. N. Dinh, Q. Yan and J. Ma, *Coord. Chem. Rev.*, 2019, **397**, 138–167.
14 Y. Liu, C. Xiang, H. Chu, S. Qiu, J. McLeod, Z. She, F. Xu, L. Sun and Y. Zou, *J. Mater. Sci. Technol.*, 2020, **37**, 135–142.
15 D.-G. Wang, Z. Liang, S. Gao, C. Qu and R. Zou, *Coord. Chem. Rev.*, 2020, **404**, 213093.
16 M. Z. Iqbal, S. S. Haider, S. Siddique, M. R. A. Karim, S. Zakar, M. Tayyab, M. M. Faisal, M. Sulman, A. Khan and M. Baghayeri, *J. Energy Storage*, 2020, **27**, 101056.
17 H. Liang, T. Lin, S. Wang, H. Jia, C. Li, J. Cao, J. Feng, W. Fei and J. Qi, *Dalton Trans.*, 2020, **49**, 196–202.
18 G. Xia and S. Wang, *Ceram. Int.*, 2019, **45**, 20810–20817.
19 W. Chen, P. Yuan, S. Guo, S. Gao, J. Wang, M. Li, F. Liu, J. Wang and J. Cheng, *J. Electroanal. Chem.*, 2019, **836**, 134–142.
20 W. Liu, H. Niu, J. Yang, K. Cheng, K. Ye, K. Zhu, G. Wang, D. Cao and J. Yan, *Chem. Mater.*, 2018, **30**, 1055–1068.
21 X. Y. Yu and X. W. Lou, *Adv. Energy Mater.*, 2018, **8**, 1701592.
22 M. Z. Iqbal and J. Khan, *Electrochim. Acta*, 2021, **368**, 137529.
23 R. Bendi, V. Kumar, V. Bhavanasi, K. Parida and P. S. Lee, *Adv. Energy Mater.*, 2016, **6**, 1501833.
24 X. Li, A. M. Elshahawy, C. Guan and J. Wang, *Small*, 2017, **13**, 1701530.
25 X. Li, X. Xiao, Q. Li, J. Wei, H. Xue and H. Pang, *Inorg. Chem. Front.*, 2018, **5**, 11–28.

26 M. Z. Iqbal, M. M. Faisal, S. R. Ali, A. M. Afzal, M. R. A. Karim, M. A. Kamran and T. Alharbi, *Ceram. Int.*, 2020, **46**, 10203–10214.

27 M. Z. Iqbal, A. Khan, A. Numan, S. S. Haider and J. Iqbal, *Ultrason. Sonochem.*, 2019, **59**, 104736.

28 M. Z. Iqbal, J. Khan, S. Siddique, A. M. Afzal and S. Aftab, *Int. J. Hydrogen Energy*, 2021, **46**, 15807–15819.

29 S. Alam, M. Z. Iqbal and J. Khan, *Int. J. Energy Res.*, 2021, **45**, 11109–11122.

30 M. Pramanik, R. R. Salunkhe, M. Imura and Y. Yamauchi, *ACS Appl. Mater. Interfaces*, 2016, **8**, 9790–9797.

31 A. A. Mirghni, M. J. Madito, T. M. Masikhwa, K. O. Oyedotun, A. Bello and N. Manyala, *J. Colloid Interface Sci.*, 2017, **494**, 325–337.

32 K. Raju, H. Han, D. B. Velusamy, Q. Jiang, H. Yang, F. P. Nkosi, N. Palaniyandy, K. Makgopa, Z. Bo and K. I. Ozoemena, *ACS Energy Lett.*, 2019, **5**, 23–30.

33 H. C. Chen, S. Jiang, B. Xu, C. Huang, Y. Hu, Y. Qin, M. He and H. Cao, *J. Mater. Chem. A*, 2019, **7**, 6241–6249.

34 M. Z. Iqbal, J. Khan, A. M. Afzal and S. Aftab, *Electrochim. Acta*, 2021, 138358.

35 X. Chen, M. Cheng, D. Chen and R. Wang, *ACS Appl. Mater. Interfaces*, 2016, **8**, 3892–3900.

36 Y.-C. Chen, Z.-B. Chen, Y.-G. Lin and Y.-K. Hsu, *ACS Sustainable Chem. Eng.*, 2017, **5**, 3863–3870.

37 N. Duraisamy, N. Arshid, K. Kandiah, J. Iqbal, P. Arunachalam, G. Dhanaraj, K. Ramesh and S. Ramesh, *J. Mater. Sci.: Mater. Electron.*, 2019, **30**, 7435–7446.

38 J. Theerthagiri, K. Thiagarajan, B. Senthilkumar, Z. Khan, R. A. Senthil, P. Arunachalam, J. Madhavan and M. Ashokkumar, *ChemistrySelect*, 2017, **2**, 201–210.

39 Y. Zhao and C.-a. Wang, *J. Alloys Compd.*, 2016, **677**, 281–287.

40 Y. Zhao, S. Li and C.-a. Wang, *ECS J. Solid State Sci. Technol.*, 2015, **5**, M5.

41 Y. Zhao and C.-A. Wang, *Mater. Des.*, 2016, **97**, 512–518.

42 Y.-H. Dai, L.-B. Kong, K. Yan, M. Shi, Y.-C. Luo and L. Kang, *Ionics*, 2016, **22**, 1461–1469.

43 B. Mahmoud, A. Mirghni, K. Oyedotun, D. Momodu, O. Fasakin and N. Manyala, *J. Alloys Compd.*, 2020, **818**, 153332.

44 X. Peng, H. Chai, Y. Cao, Y. Wang, H. Dong, D. Jia and W. Zhou, *Mater. Today Energy*, 2018, **7**, 129–135.